Peridynamic modeling of fracture in fiber-reinforced composites

Amin Yaghoobi*, Mi G. Chorzepa

College of Engineering, University of Georgia, Athens, GA 30602, USA

Abstract

This paper studies the effect of fiber volume fraction and fiber length on fracture behaviour of reinforced concrete structures. Cementitious material is modeled using the non-ordinary state-based peridynamic theory. The non-local meshfree peridynamic method unifies mechanics of continuous and discontinuous media and thus is well-suited in simulating discontinuities such as cracks compared to the traditional mesh-based finite element method. In addition, the non-ordinary state-based peridynamics enables us to incorporate classical constitutive equations and damage criterion. Furthermore, in order to incorporate fiber within the cementitious composite, a modified semi-discrete model is introduced. A two-dimensional rectangular notched model is developed to study the effect of fiber amount and fiber length on mechanical response of cementitious composite and also on damage propagation pattern. Sufficient number of simulations are performed to statistically characterize the effect of fiber reinforcement on fracture behaviour of cementitious composite structures.

Keywords: Peridynamics; Fiber volume fraction; Fiber length; Fracture behaviour.

1. Introduction

Addition of fibers improves tensile strength, ductility and load carrying capacity of cementitious materials [1, 2]. The performance of fiber reinforced cementitious (FRC) structures is dependent on the fiber volume fraction, orientation, and spatial distribution [3, 4]. Therefore, it is important to

*Corresponding author

develop practical analytical methods to investigate different parameters that affect the strength of FRC structures. Studies on FRC structures are mostly limited to the finite element analysis (FEA) framework [5–7]. However, the FEA has some deficiencies which play an important role in FRC simulations. First of all, FEA fails to model the interface or bond between dissimilar materials. Also, external failure criterions are needed for crack initiation and propagation. Crack growth is generally predicted, and remeshing elements is necessary during the failure process. In recent years, nonlocal meshfree methods have been an alternative to the FEA in various continuum mechanics applications, particularly in fracture mechanics.

The peridynamics, first introduced by Silling [8], is a reformulation of the classical continuum mechanics in terms of integro-differential equations, and thus is valid anywhere in a deformable body regardless of any discontinuity. The peridynamic method discretizes the background medium into particles and represents the material model by defining the bond between particle points selected within a finite distance, referred to as 'horizon'. The original peridynamics, known as bond-based peridynamics (BBPD), is limited to modeling materials with a Poissons ratio of 1/4 [9]. Gerstle et al. [10] enhanced BBPD by allowing the bond of two material points to carry not only pairwise forces, but also peridynamic moments. The resulting model, called micropolar peridynamics (MPPD), can simulate linear elastic materials with varying Poissons ratios. BBPD and MPPD have been primarily used for a fracture analysis of plain and reinforced concrete members under quasi-static [11–14] and impact loading [15, 16].

Non-ordinary state-based peridynamics (NOSBPD) is the most generalized form of the peridynamics in which the mechanics of given point depends on the deformation state of all bonds established by surrounding points. NOSBPD can use any material model by incorporating the classical constitutive equations and classical damage criteria [17, 18]. Breitenfeld et al. [19] developed a NOSBPD discretization scheme for linear elastic materials and performed two-dimensional (2D) and three-dimensional (3D) stationary crack problems. Tupek et al. [20] introduced an approach that incorporates a classical damage criterion within the NOSBPD framework and applied to the simulation of a ballistic impact on aluminum panels.

Yaghoobi and Chorzepa [21] proposed a meshless analysis framework based on NOSBPD to predict the response of FRC structures. NOSBPD unifies the mechanics of continuous and discontinuous media and enables the use of classical constitutive equations and classical damage criteria. In order to incorporate fibers within the cementitious matrix, a semi-discrete model is used in which the fiber-matrix reaction is applied to the matrix material points. The fiber-matrix reaction force, refer to as the fiber force for short, is assumed to be equal to the fiber pull-out force obtained from a micro-mechanical model. The meshless framework has been verified and validated through several examples. Later, Yaghoobi and Chorzepa [22] modified the meshless FRC modeling and studied the fracture behaviour of three point bending FRC beam with an asymmetric notch to demonstrate the effectiveness of the proposed framework in modeling unguided and complex crack patterns.

In this paper, the meshless framework introduced by Yaghoobi and Chorzepa [21] has been modified in order to incorporate the effect of fiber volume fraction, fiber length and fiber distribution in fracture analysis of FRC structures. A 2D model is provided with symmetric notches to investigate indistinctive damage growth path. Numerical results indicate that the proposed methodology improves the prediction of a crack growth path in complex cementitious composite structures. Furthermore, results show that addition of fibers improves the load carrying capacity of FRC samples by transferring loads from the stress concentration area and distributing to other areas. With the same fiber volume fraction, the results indicate that greater peak load resulted from longer fiber length.

2. Non-ordinary state-based peridynamics

Dynamics of a given point $\mathbf{x}_i$ in the NOSBPD formulation, depend on deformation of all bonds surrounding the point. Vector-states are introduced to describe the kinematics of the body (see Fig. 1). For example, the position vector-state $\mathbf{X}$, also called the bond $\boldsymbol{\xi}$, from the perspective of $\mathbf{x}_i$, is defined as the relative position of $\mathbf{x}_i$ and $\mathbf{x}_j$ in the reference configuration $\mathbf{B}_0$.

$$\mathbf{X}\langle \mathbf{x}_j - \mathbf{x}_i \rangle = \mathbf{x}_j - \mathbf{x}_i = \boldsymbol{\xi}_{ij} \tag{1}$$

The deformation vector-state, $\mathbf{Y}$, represents the bond in the deformed body $\mathbf{B}$.

$$\mathbf{Y}\langle \mathbf{x}_j - \mathbf{x}_i \rangle = \mathbf{y}_j - \mathbf{y}_i \tag{2}$$

where $\mathbf{y}_i = \mathbf{x}_i + \mathbf{u}_i$ and $\mathbf{y}_j = \mathbf{x}_j + \mathbf{u}_j$. $\mathbf{u}_i$ and $\mathbf{u}_j$ are deformations corresponding to $\mathbf{x}_i$ and $\mathbf{x}_j$, respectively. Fig. 1 depicts a schematic for peridynamic states. Indices indicate the correspondence of a variable to material points, $\mathbf{A}_i$ denotes the state $\mathbf{A}$ at point $\mathbf{x}_i$, or $\mathbf{A}_{ij}$ corresponds to the bond between $\mathbf{x}_i$ and $\mathbf{x}_j$. It is also worth mentioning that in NOSBPD, the deformation vector-state, $\mathbf{Y}$, takes the role of deformation gradient tensor, $\mathbf{F}$, in classical local mechanics in describing kinematics of the body [21, 23]. Silling [23] introduced an approximation for evaluating the classical deformation gradient tensor in order to incorporate the classical constitutive equations in NOSBPD.

$$\mathbf{F}_i = [\sum_{j=1}^{N_i} \omega_{ij} \left(\mathbf{y}_j - \mathbf{y}_i\right) \otimes \left(\mathbf{x}_j - \mathbf{x}_i\right) \mathrm{d}V_j].\mathbf{K}_i^{-1} \tag{3}$$

where ω_{ij} denotes an influence function and N_i is the number of points within the horizon of $\mathbf{x}_i$. $\mathbf{K}$ a is shape tensor, expressed as follows at point $\mathbf{x}_i$.

$$\mathbf{K}_i = \sum_{j=1}^{N_i} \omega_{ij} \left(\mathbf{x}_j - \mathbf{x}_i\right) \otimes \left(\mathbf{x}_j - \mathbf{x}_i\right) \mathrm{d}V_j \tag{4}$$

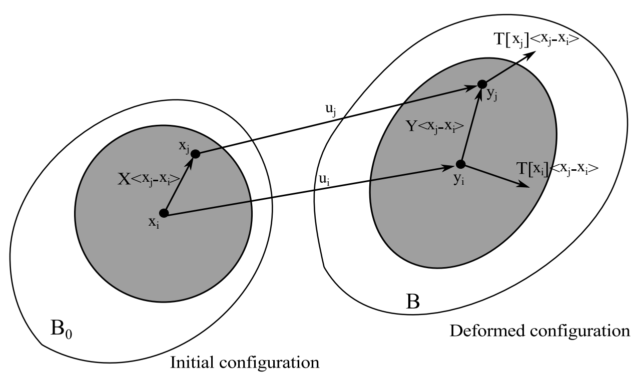

Figure 1: Peridynamic states: Position vector-state $\mathbf{X}$, deformation vector-state $\mathbf{Y}$, and force vector-state $\mathbf{T}$.

In NOSBPD, it is assumed that points interact through long-range forces represented by force vector-state $\mathbf{T}$ [23]. The steady-state equilibrium equations for point $\mathbf{x}_i$ is given by summation of force vector-states over the horizon of $\mathbf{x}_i$

$$\sum_{j=1}^{N_i} \{\mathbf{T}_i\langle\mathbf{x}_j - \mathbf{x}_i\rangle - \mathbf{T}_j\langle\mathbf{x}_i - \mathbf{x}_j\rangle\}\mathrm{d}V_j + \mathbf{b}_i = 0 \tag{5}$$

where $\mathbf{b}$ is the body force and V_j is the volume of point $\mathbf{x}_j$. The force vector-state is obtained from

$$\mathbf{T}_i\langle \mathbf{x}_j - \mathbf{x}_i \rangle = \omega_{ij} \boldsymbol{\sigma}_i \mathbf{K}_i^{-1} (\mathbf{x}_j - \mathbf{x}_i) \tag{6}$$

where $\boldsymbol{\sigma}$ is the first Piola-Kirchhoff stress and determined through material constitutive equation.

2.1. Formulation of the force vector-state

The discretization of force vector-state is provided by Breitenfeld et al. [19], and Yaghoobi and Chorzepa [21]. This study presents a modified formulation for a 2D plane stress problem. For linearly elastic materials with small deformations, the infinitesimal strain tensor $\boldsymbol{\epsilon} = 0.5(\mathbf{F}^T + \mathbf{F}) - \mathbf{I}$ can be rewritten by definition of peridynamic deformation gradient tensor (Eq. 3) as

$$\boldsymbol{\epsilon}_i = 1/2[\sum_{j=1}^{N_i} \omega_{ij} \{(\mathbf{u}_j - \mathbf{u}_i) \otimes (\mathbf{x}_j - \mathbf{x}_i) + (\mathbf{x}_j - \mathbf{x}_i) \otimes (\mathbf{u}_j - \mathbf{u}_i)\} \mathrm{d}V_j].\mathbf{K}_i^{-1} \tag{7}$$

The infinitesimal strain tensor in vector (or Voigt) notation takes the following form,

$$\boldsymbol{\epsilon}_i = \mathbf{K}_i^* \sum_{j=1}^{N_i} \omega_{ij} \mathbf{N}_{ij} \mathbf{U}_{ij} \mathrm{d}V_j \tag{8}$$

where for a 2D problem, $\mathbf{K}^*$ is a 3×4 matrix and stores the arrays of inverse of shape tensor $\mathbf{K}$.

$$\mathbf{K}_i^* = \begin{bmatrix} K_{11}^{-1} & 0 & K_{12}^{-1} & 0 \\ 0 & K_{12} & 0 & K_{22}^{-1} \\ K_{12}^{-1} & K_{11}^{-1} & K_{22}^{-1} & K_{12}^{-1} \end{bmatrix} \tag{9}$$

$\mathbf{N}$ is a 4×2 matrix which formed form arrays of position vector-state $\boldsymbol{\xi}_{ij} = [\xi_1, \xi_2] = \mathbf{x}_j - \mathbf{x}_i$, as show below:

$$\mathbf{N} = \begin{bmatrix} \xi_1 & 0 \\ 0 & \xi_1 \\ \xi_2 & 0 \\ 0 & \xi_2 \end{bmatrix} \tag{10}$$

and $\mathbf{U}_{ij} = \mathbf{u}_j - \mathbf{u}_i$ is the relative deformation vector. The material behavior of concrete is assumed to be linear elastic, and strain softening occurs once the concrete damages. An exponential damage model is selected to represent the strain softening and thus is used in defining the constitutive equation [24]:

$$\boldsymbol{\sigma} = (1 - D)\,\mathbf{C} : \boldsymbol{\epsilon} \tag{11}$$

where $\mathbf{C}$ is the plain stress isotropic elastic moduli matrix,

$$\mathbf{C} = \frac{E}{(1+\nu)(1-2\nu)} \begin{bmatrix} 1-\nu & \nu & 0 \\ \nu & 1-\nu & 0 \\ 0 & 0 & 1/2(1-2\nu) \end{bmatrix} \tag{12}$$

D is the damage variable ranging from zero to one, and is described as an exponential function of ϵ_{eq}, the largest equivalent strain and determined by

$$D = \begin{cases} 0 & : \epsilon_{eq} < \epsilon_0 \\ 1 - \frac{\epsilon_0}{\epsilon_{eq}} e^{-\frac{\epsilon_{eq}-\epsilon_0}{\epsilon_f - \epsilon_0}} & : \epsilon_{eq} \geq \epsilon_0 \end{cases} \tag{13}$$

where $\epsilon_0 = f_t/E$, f_t is the tensile strength; E is the Young's modulus; ϵ_f is the parameter affecting the slope of the softening branch. The equivalent strain is based on the modified von Mises definition [25]:

$$\epsilon_{eq} = \frac{k-1}{2k\,(1-2\nu)} I_1 + \frac{1}{2k}\sqrt{\frac{(k-1)^2}{(1-2\nu)^2} I_1^2 + \frac{6k}{(1+\nu)^2} J_2} \tag{14}$$

where k represents the ratio of the compressive strength, f_c, and the tensile strength, f_t; ν denotes the Poisson's ratio, and I_1 and J_2 are the first and the second invariants of the strain tensor. To retrieve the term $\mathbf{K}_i^{-1}(\mathbf{x}_j - \mathbf{x}_i)$ in Eq. 6, $\mathbf{Q}^*$ is defined:

$$\mathbf{Q}_{ij}^* = \begin{bmatrix} Q_1 & 0 & Q_2 \\ 0 & Q_2 & Q_1 \end{bmatrix} \tag{15}$$

where $\mathbf{Q}_{ij} = [Q_1, Q_2] = \mathbf{K}_i^{-1}(\mathbf{x}_j - \mathbf{x}_i) = \mathbf{K}_i^{-1}\boldsymbol{\xi}_{ij}$. Finally, the force vector-state is obtained by

$$\mathbf{T}_i\langle \mathbf{x}_j - \mathbf{x}_i \rangle = \omega_{ij} \mathbf{Q}_{ij}^* \boldsymbol{\sigma}_i \tag{16}$$

An incremental-iterative method is developed to obtain the steady-state solution for system of NOSBPD equilibrium equations. For a displacement loading increment, the dynamic relaxation method is adapted to iteratively update the displacement field. The implementation of dynamic relaxation method in solving NOSBPD equations is presented in Yaghoobi and Chorzepa [21].

2.2. Stability

Instabilities in NOSBPD analysis has been reported before in the form of unphysical propagation of damage [20, 26] and zero-energy mode [19, 27–29]. In a peridynamic body, fully damaged points are able to flow unconstrained. Therefore, consideration of the fully damaged points in computation of the peridynamic deformation gradient, $\mathbf{F}$, for material points within the horizon of fully damaged regions will results in unphysically-large strains. In order to address this issue, Tupek et al. [26] modified the influence function in order to surpass the effect of fully damaged points on the neighboring points.

$$\omega_{ij} = \omega_\xi(|\boldsymbol{\xi}_{ij}|)\omega_D(D_i, D_j) \tag{17}$$

where $\omega_\xi(|\boldsymbol{\xi}_{ij}|)$ is the radial influence function which weights the contribution from neighboring point. D_i and D_j are the values of the damage parameter at $\mathbf{x}_i$ and $\mathbf{x}_j$, respectively, and calculated from a damage criteria, here Eq. 13. $\omega_D(D_i, D_j)$ is used to remove the effect of fully damage particles and is required to be zero if either $\mathbf{x}_i$ and $\mathbf{x}_j$ is fully damaged. Tupek et al. [26] employed specific forms for the influence functions as follows:

$$\omega_\xi(|\boldsymbol{\xi}_{ij}|) = e^{-(\frac{|\boldsymbol{\xi}_{ij}|}{\delta})^2} \tag{18}$$

$$\omega_D(D_i, D_j) = \begin{cases} 1 & : \text{if } D_i > D_{cr} \text{ or } D_j > D_{cr} \\ 0 & : \text{otherwise} \end{cases} \tag{19}$$

where D_{cr} is the critical damage and is assumed as 0.99.

The zero-energy mode which is also common in other particle integration of Galerkin's weak form formulation is well defined in [19, 27]. The addition of a force-spring-like bond force into the NOSBPD force vector-state is referred in [19] as a method to control the zero-energy mode. Li et al. introduced a supplemented force state that eliminates the need for complicated parameter adjustment in [19]. Moreover, Wu and Ren [30] introduced a stabilized displacement field to surpass the zero-energy mode. This paper utilises a higher-order approximation for the nonlocal deformation gradient tensor proposed by Yaghoobi and Chorzepa [27] in order to successfully control the zero-energy mode.

3. Semi discrete fiber model

In semi-discrete modeling of the fibers within a cementitious matrix, fibers do not possess independent degrees of freedom. The fiber-matrix reaction forces are applied to the background matrix mesh. Since each individual fiber is implicitly represented, the semi-discrete model offers the advantages of a fully-discrete model in determining local behavior of the fibers and effect of fiber distribution. In addition, the semi-discrete model is computationally much more effective particularly when thousands or millions of fibers are present.

In order to model a fiber that bridges a crack, the closing forces associated with the fiber-matrix reaction are transferred to the matrix. In this paper, the fiber-matrix interaction or fiber bridging force is governed by the fiber pull-out behavior as $P(\Delta)$, where P is the fiber pull-out force and Δ is the fiber pull-out distance. Also, it is assumed that a fiber contributes to the cementitious matrix material model when it bridges a crack, where a crack is associated with damaged matrix points. Therefore, it is necessary to contribute a fiber if it crosses a damaged area. For this aim as seen in Fig. 2(a), a fiber influence area is defined including all matrix points within a finite distance from the fiber. A fiber is activated only if at minimum a point within the fiber influence area is damaged (See Fig. 2(b)). In order to activate a fiber, fiber damage parameter, D_f, is introduced. Fiber damage parameter ranges between 0 and 1 and is equal to the largest damage parameter of points around the fiber. $D_f = 0$ indicates no damage within a set of points bridged by the fiber, and thus the fiber force is not applied to the model. Whereas, $D_f > 0$ represents that at minimum one point around the fiber is damaged. In such case, the fiber is engaged in the model, and the scaled fiber force, P_f, is applied to the model.

$$P_f = D_f \; P \tag{20}$$

Lumped-forces applied to the crack surface and distributed-force along the fiber embedment are among viable assumptions to transfer the fiber bridging force to the cementitious matrix. Yaghoobi and Chorzepa [22] assumed that the fiber force is uniformly distributed to matrix points within the fiber influence area as shown in Fig. 2(a). Details for fiber force calculations and the methodology to distribute the fiber force to the matrix points are also given in [22].

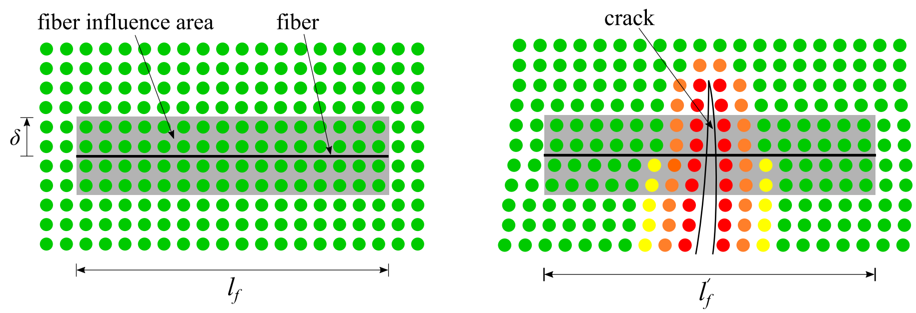

(a) fiber in undeformed body

(b) fiber bridging a damaged area

Figure 2: Schematic for fiber activation and fiber force distribution.

4. Numerical results

The mechanical response and fracture behavior of cementitious composites is highly affected by its matrix and fiber material properties, fiber type, fiber amount and spatial distribution of fibers as well as the distribution of initial imperfections from pre-existing cracks and pores. In addition, the complexity and inconsistency of damage growth pattern makes it difficult to study FRC composites with the traditional FEA method. On the other hand, peridynamics unifies the mechanics of continuous media, cracks, and discrete points and does not have the need for an extra criteria to nucleate cracks or to determine a crack growth path. These features, along with the nonlocal effect of fibers in FRC composites, make the proposed nonlocal approach, a powerful and convenient tool for a failure analysis of FRC composites. A 2D model (see Fig. 3) is developed to investigate the effect of fiber amount and fiber length on the fracture behavior of FRC structures. In order to localize the damage, two symmetric notches have been provided in the model (2 mm in depth and 2 mm in width). The model is restrained at one side and pulled from the other side. Displacement conditions are applied to the shaded areas (5 mm in width at both ends) as shown in Fig. 3.

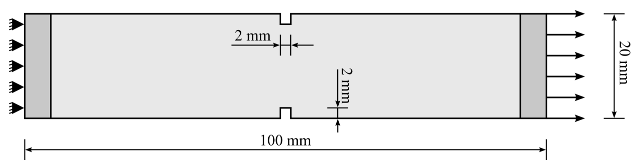

Figure 3: 2D pre-notched plate under tension.

The mechanical properties of cementitious matrix are highly affected by the percentage proportions of the matrix ingredients. In this work, the mechanical properties of cementitious matrix are taken as: $E = 20000\ MPa$, $\nu = 0.18$, $f_t = 3\ MPa$ and $f_c = 30MPa$. The softening parameter, ϵ_f, is assumed to be 0.01.

4.1. Mesh refinement

In the first step, a convergence study is performed to obtain an effective discretization scheme for the plain cementitious matrix. In the convergence study, four types of peridynamic discretization scheme are used with varying spacing size, $h = 2\ mm$, $h = 1\ mm$, $h = 0.66\ mm$ and $h = 0.5\ mm$. In all cases, the horizon size, δ, is assumed to $3.015h$. This value has been reported to ensure the nonlocality of failure at an acceptable computational expense [8]. Furthermore, in the convergence study, a modification on damage model is applied as follows, in order to minimize the effect of mesh sensitivities:

$$\bar{\epsilon}_f = \frac{1}{h}(\epsilon_f - 0.5\epsilon_f) + 0.5\epsilon_f \tag{21}$$

Nothing that as suggested in [31], initial imperfections from pores and shrinkage are represented by reducing concrete strength of arbitrarily selected points. Thus, the tensile strength of 5% of points is reduced by 25% and another 5% are reduced by 50%. The weak points are selected arbitrary using uniform random generators. An example for weak particles map is provided in Fig. 4. For each spacing size, 60 different runs are performed to statistically analyze weak point distribution on load carrying capacity of plain concrete models.

The load-displacement curves obtained from peridynamic simulations are provided in Fig. 5. The mean curve is also provided. As seen in Fig. 5 for all spacing sizes, the maximum load capacity (or peak force) and the softening part are slights affected with the random selection of the weak particles. The mean curves for four different particle spacing size are compared in

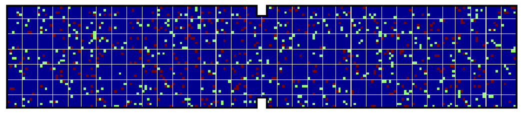

Figure 4: Schematic map of weak points for $h = 0.5\ mm$, the strength of Green and Red points are reduced by 25% and 50%, respectively.

Fig. 6. Furthermore, the probability function of the peak load and the variation of mean peak force by sample number are provided in Figs. 7(a) and 7(b). As seen in the figures, for smaller spacing sizes of $h = 0.66\ mm$ and $h = 0.50\ mm$, results are converging. Although decreasing spacing size means increasing number of points and then computational expense, hereinafter to study the effect of fibers on damage behavior of FRC structures, the discretization with $h = 0.50\ mm$ is used for accuracy.

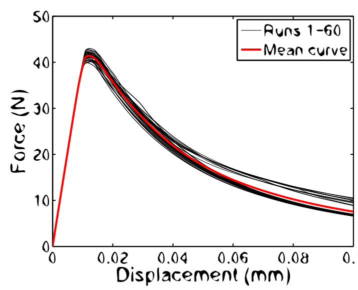

(a) $h = 2.00\ mm$

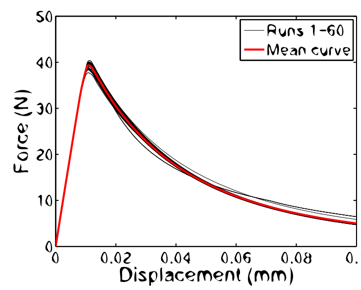

(b) $h = 1.00\ mm$

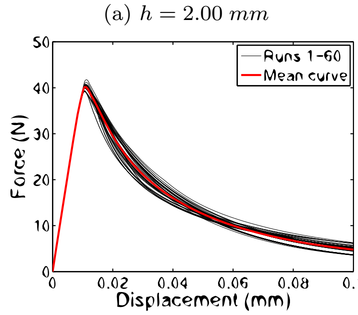

(c) $h = 0.66\ mm$

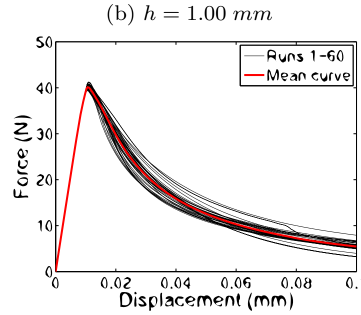

(d) $h = 0.50\ mm$

Figure 5: Load-deflection curves of plain concrete for different spacing sizes.

To study how the fiber addition affects the performance of a FRC structure, five sets of FRC models are developed with varying number of fibers and fiber length as in Table 1. Noting that for each case, the corresponding fiber volume fraction, v_f, is obtained via V_f/V_t. $V_f = N_f l_f \pi d_f^2/4$ is the

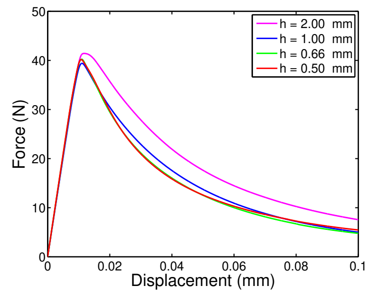

Figure 6: Mean loaddisplacement curves for different spacing sizes.

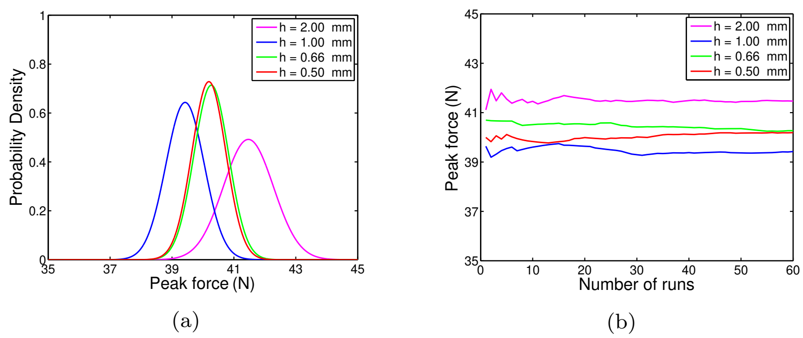

Figure 7: (a) Probability function of the peak load, (b) effect of the sample number on the mean peak load.

total fiber volume, where N_f, l_f and d_f are the number of fibers, the fiber length and the fiber diameter, respectively. The plate volume is obtained for the plane-stress state with thickness of 1 mm. The parameters of micromechanical pull-out force are adopted from [22]. Fig. 8 represents the spatial distribution of fibers for FRC models in Table 1. Fibers are arbitrary positioned within the plate using a uniform distributed random numbers. As in convergence study, in order to take into account the stochastic character of weak points and fiber distributions, 60 runs (for a FRC model in Table 1) are performed in which weak points and fiber distributions are selected randomly.

4.2. Effect of number of fibers

Fig. 9 depicts the load-displacement curves for FRC1, FRC2 and FRC3. Mean load-displacement curves for FRC1, FRC2 and FRC3 are compared in Fig. 10. It is clearly illustrated that increased number of fibers (or volume fraction) increases the peak load carried by the cementitious matrix.

FRC Model	Number of fibers, N_f	Fiber length, l_f (mm)	Fiber volume fraction (%)
FRC1	20	16	0.5
FRC2	40	16	1.0
FRC3	60	16	1.5
FRC4	53	12	1.0
FRC5	80	8	1.0

Table 1: Number of fibers and fiber length used in the FRC models

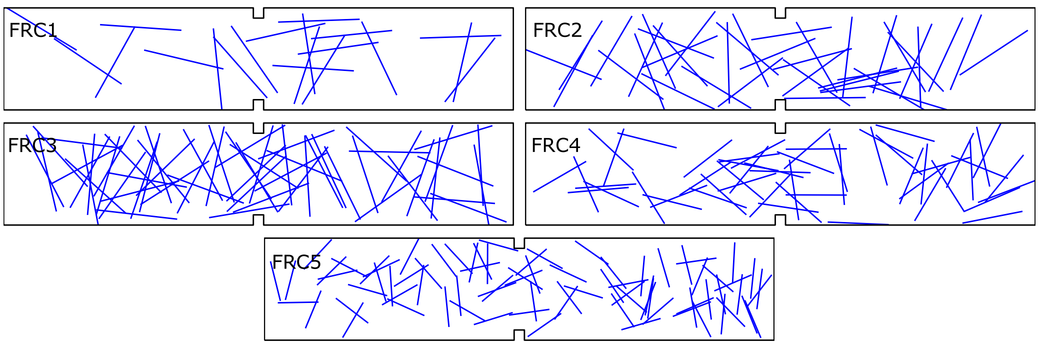

Figure 8: Samples of fiber distribution for FRC cases in Table 1

The probability function of the peak load and the residual load at displacement loading of 0.1 mm are provided in Figs. 11(a) and 12(a), respectively. It is clearly illustrated that by increasing number of fibers (or volume fraction) the deviation from the mean value is increasing. Therefore, for higher fiber amount, the fiber distribution plays more important role to characterize the FRC models. Figs. 11(b) and 12(b) study the effect of the simulation number on the mean peak load and mean residual load. For all three cases of FRC1, FRC2 and FRC3, the results converge when 40 or more simulations are performed. Therefore, the sample size of 60 provides statistically sufficient number of simulations.

4.3. Effect of fiber length

In this section, for a constant value of fiber volume fraction, the effect of fiber length is studied on load carrying capacity and fracture behaviour of FRC composites. Varying fiber length, to achieve a constant fiber volume fraction, number of fibers needs to be adjusted. In addition to FRC2 (l_f = 16 mm and N_f = 40), two other FRC model sets of FRC4 (l_f = 12 mm and N_f = 53) and FRC5 (l_f = 8 mm and N_f = 80) are provided. The corresponded fiber volume fraction for all three cases is $v_f = 1.0\%$. The load-

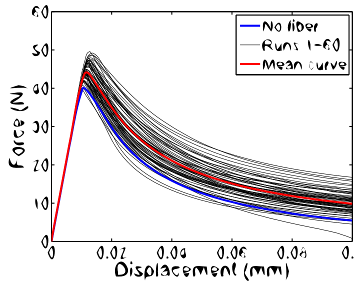

(a) FRC1, $N_f = 20$

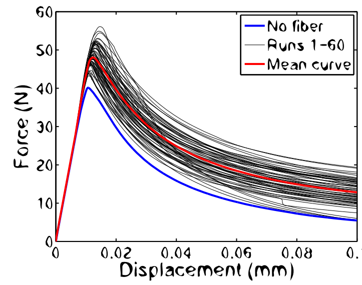

(b) FRC2, $N_f = 40$

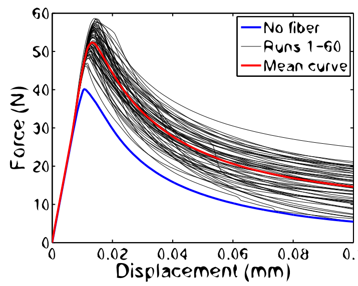

(c) FRC3, $N_f = 60$

Figure 9: Load-deflection curves of fiber reinforced concrete for different fiber numbers.

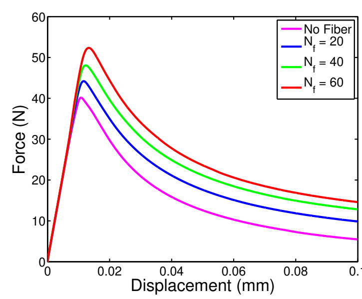

Figure 10: Mean loaddisplacement curves for different fiber numbers.

displacement curves of 60 different runs are provided in Figs. (a) and (b) for FRC4 and FRC5, respectively. Furthermore, the mean load-displacement curves for FRC2, FRC4 and FRC5 are illustrated in Fig. 14. Although three sets represents the same fiber volume fraction, the figure indicates that greater peak load resulted from longer fiber length.

The probability function of the peak load and the residual load at displacement loading of 0.1 mm are provided in Figs. 15(a) and 16(a), respectively. Figs. 15(b) and 16(b) study the effect of the simulation number on

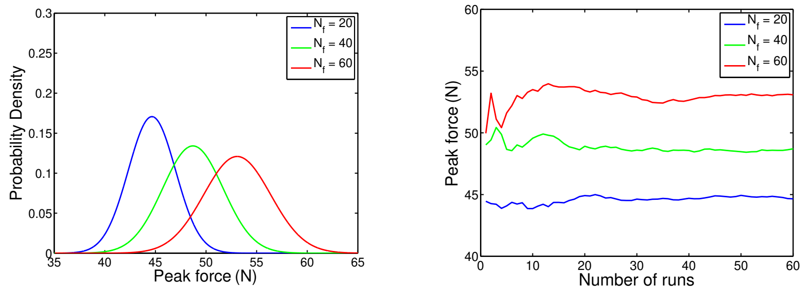

(a) (b)

Figure 11: (a) Probability function of the peak load, (b) effect of the sample number on the mean peak load, for different fiber numbers.

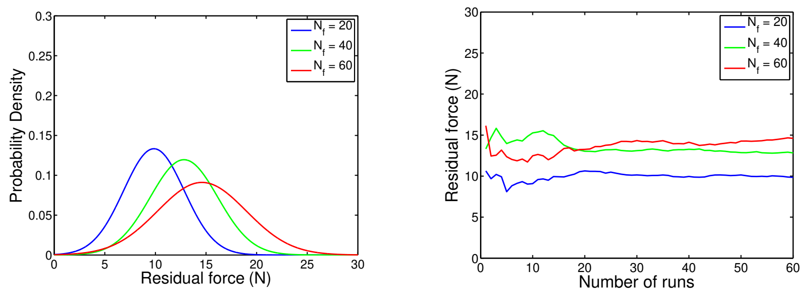

(a) (b)

Figure 12: (a) Probability function of the peak load, (b) effect of the sample number on the mean peak load, for different fiber numbers.

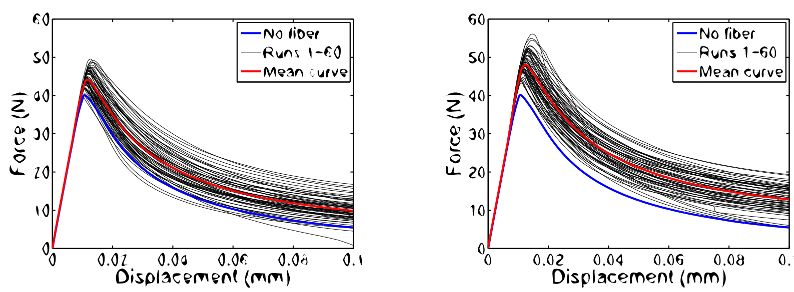

(a) FRC4, $l_f = 12\ mm$ (b) FRC5, $l_f = 8\ mm$

Figure 13: Load-deflection curves of fiber reinforced concrete for different fiber numbers.

the mean peak load and mean residual load.

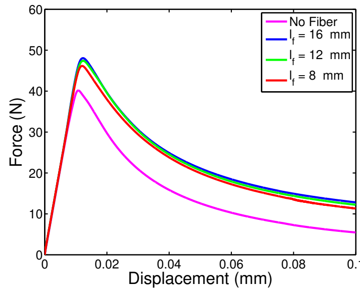

Figure 14: Mean loaddisplacement curves for different fiber numbers.

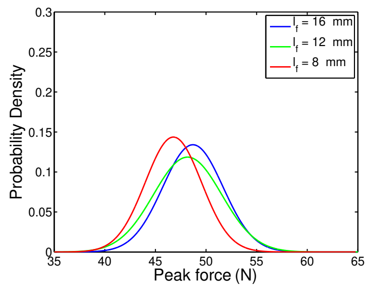

(a)

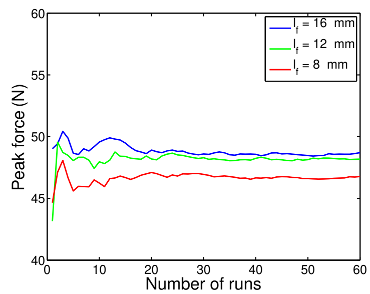

(b)

Figure 15: (a) Probability function of the peak load, (b) effect of the sample number on the mean peak load, for different fiber numbers..

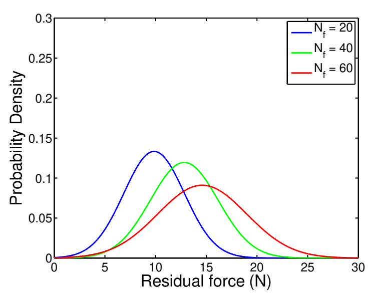

(a)

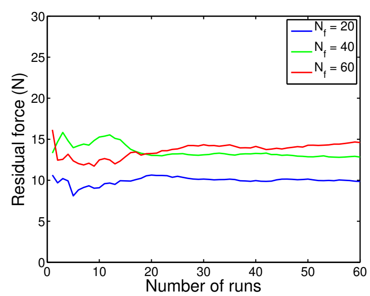

(b)

Figure 16: (a) Probability function of the peak load, (b) effect of the sample number on the mean peak load, for different fiber numbers.

4.4. Damage patterns

Fig. 17 presents a comparison between damage patterns from four cases of plain concrete, FRC1, FRC2 and FRC3. For each case, the damage pattern of four selected simulation are provided from the total of 60 simulations.

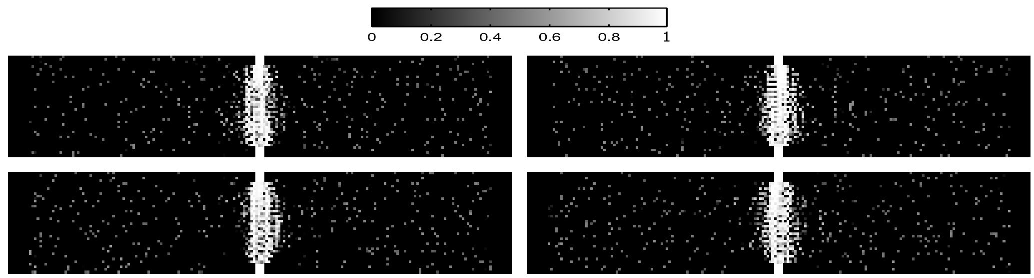

(a) No fiber, $v_f = 0\%$

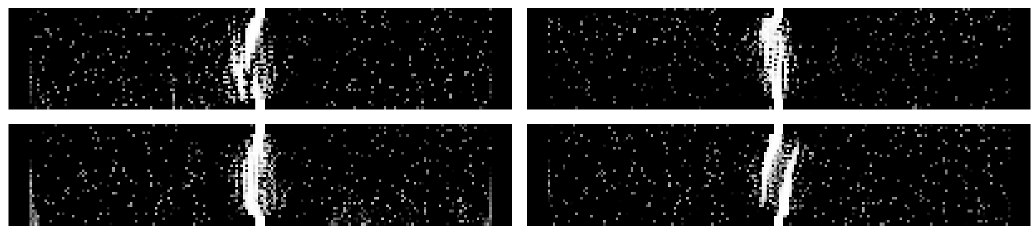

(b) FRC1, $v_f = 0.5\%$

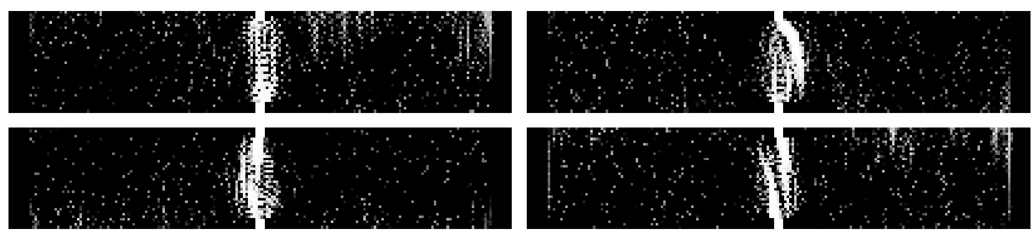

(c) FRC2, $v_f = 1.0\%$

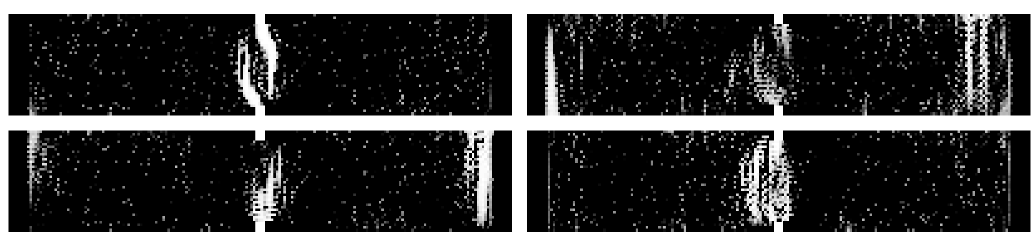

(d) FRC3, $v_f = 1.5\%$

Figure 17: Damage patterns for varying fiber volume fraction at 0.1 mm displacement loading

The figure indicates that the damage pattern for the plain concrete models includes damaged particles concentrated in the localized area between the notches. However, by increasing the number of fibers (or volume fraction), the damaged area is extended to a larger area. In some samples, two discrete

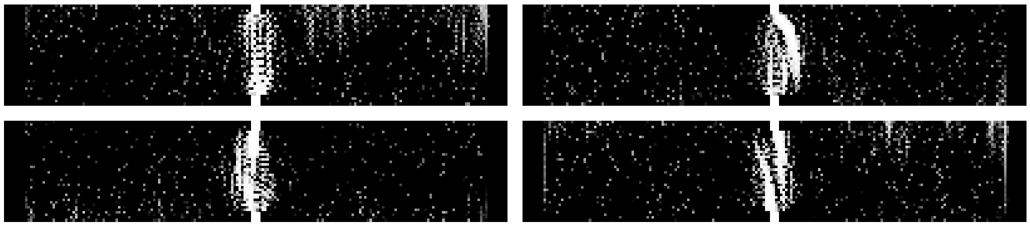

(a) FRC2, $l_f = 16\ mm$

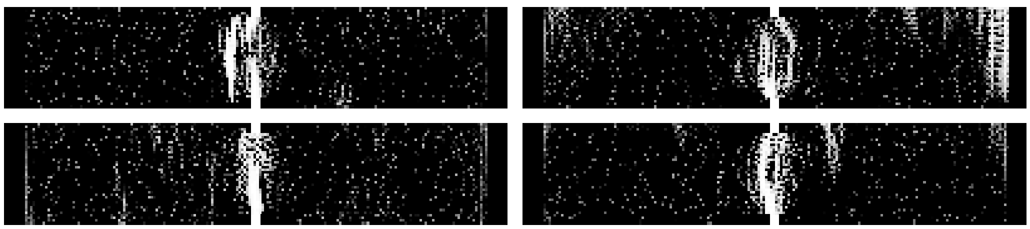

(b) FRC4, $l_f = 12\ mm$

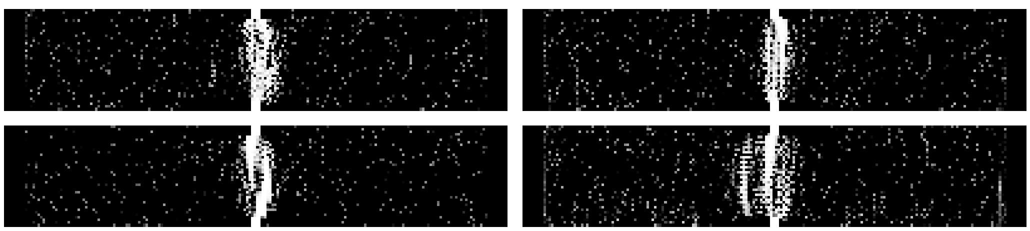

(c) FRC5, $l_f = 8\ mm$

Figure 18: Damage patterns for varying fiber length at 0.1 mm displacement loading

cracks are developed or the damage is occurred away from the localized area. These results prove the fact that fibers can improve the fracture behaviour of FRC composites by transferering loads from stress concentration area to other parts.

The damage patterns presented in Fig. 18 are for the cases in Section 4.3 to study the effect of fiber length. The damage patterns for FRC4 ($l_f =$ 12 mm and $N_f = 53$) resemble the damage patterns for FRC2 ($l_f = 16\ mm$ and $N_f = 40$). However, the damage patterns for FRC5 ($l_f = 8\ mm$ and $N_f = 80$) are more concentrated to the localized area. In other word, with the same fiber volume fraction, larger fibers are more effective in transferring the load from the stress concentrations, and then effectively improve the load carrying capacity of a FRC specimen.

5. Conclusion

The failure behavior of the fiber reinforced (FRC) structures is characterized in the peridynamic analysis framework. A semi-discrete model is developed within the non-ordinary state-based peridynamic framework. The definition of a nonlocal deformation gradient enables the use of the classical constitutive equations and damage models in the non-ordinary state-based peridynamic framework. Furthermore, the proposed semi-discrete model considers modeling the effect of individual fibers at an acceptable computational cost. The dynamic relaxation method is used to solve nonlinear peridynamic equations. The proposed approach enables to perform statistical analysis to characterize the FRC composites. The meshless peridynamic simulations of a notched FRC structure are performed to study the effect of fiber volume fraction and fiber length on fracture behaviour of FRC composites. It is clearly illustrated that addition of fibers improves the load carrying capacity of FRC samples by transferring loads from the stress concentration area and distributing to other areas. Furthermore, with the same fiber volume fraction, the results indicate that greater peak load resulted from longer fiber length.

References

[1] R. F. Zollo, Fiber-reinforced concrete: an overview after 30 years of development, Cement and Concrete Composites 19 (2) (1997) 107–122.

[2] J. Gao, W. Sun, K. Morino, Mechanical properties of steel fiber-reinforced, high-strength, lightweight concrete, Cement and Concrete Composites 19 (4) (1997) 307–313.

[3] P. Soroushian, C.-D. Lee, Distribution and orientation of fibers in steel fiber reinforced concrete, Materials Journal 87 (5) (1990) 433–439.

[4] P. Soroushian, Z. Bayasi, Fiber type effects on the performance of steel fiber reinforced concrete, Materials Journal 88 (2) (1991) 129–134.

[5] A. Carpinteri, R. Brighenti, Fracture behaviour of plain and fiber-reinforced concrete with different water content under mixed mode loading, Materials & Design 31 (4) (2010) 2032–2042.

[6] R. Hameed, A. Sellier, A. Turatsinze, F. Duprat, Metallic fiber-reinforced concrete behaviour: Experiments and constitutive law for finite element modeling, Engineering Fracture Mechanics 103 (2013) 124–131.

[7] J. Kang, K. Kim, Y. M. Lim, J. E. Bolander, Modeling of fiber-reinforced cement composites: Discrete representation of fiber pullout, International Journal of Solids and Structures 51 (10) (2014) 1970–1979.

[8] S. A. Silling, E. Askari, A meshfree method based on the peridynamic model of solid mechanics, Computers & Structures 83 (17) (2005) 1526–1535.

[9] E. Madenci, E. Oterkus, Peridynamic theory and its applications, Vol. 17, Springer, 2014.

[10] W. Gerstle, N. Sau, S. Silling, Peridynamic modeling of plain and reinforced concrete structures, in: SMiRT18, Int. Conf. Structural Mech. Reactor Technol, 2005.

[11] W. Gerstle, N. Sau, S. Silling, Peridynamic modeling of concrete structures, Nuclear engineering and design 237 (12) (2007) 1250–1258.

[12] W. Gerstle, N. Sau, E. Aguilera, Micropolar peridynamic modeling of concrete structures, in: Proceedings of the 6th international conference on fracture mechanics of concrete structures, 2007.

[13] W. Gerstle, N. Sau, N. Sakhavand, On peridynamic computational simulation of concrete structures, ACI Special Publication 265.

[14] B. Kilic, E. Madenci, Prediction of crack paths in a quenched glass plate by using peridynamic theory, International journal of fracture 156 (2) (2009) 165–177.

[15] S. A. Silling, E. Askari, Peridynamic modeling of impact damage, in: ASME/JSME 2004 Pressure Vessels and Piping Conference, American Society of Mechanical Engineers, 2004, pp. 197–205.

[16] A. Agwai, I. Guven, E. Madenci, Peridynamic theory for impact damage prediction and propagation in electronic packages due to drop, in: Electronic Components and Technology Conference, 2008. ECTC 2008. 58th, IEEE, 2008, pp. 1048–1053.

[17] S. A. Silling, M. Epton, O. Weckner, J. Xu, E. Askari, Peridynamic states and constitutive modeling, Journal of Elasticity 88 (2) (2007) 151–184.

[18] T. L. Warren, S. A. Silling, A. Askari, O. Weckner, M. A. Epton, J. Xu, A non-ordinary state-based peridynamic method to model solid material deformation and fracture, International Journal of Solids and Structures 46 (5) (2009) 1186–1195.

[19] M. Breitenfeld, P. Geubelle, O. Weckner, S. Silling, Non-ordinary state-based peridynamic analysis of stationary crack problems, Computer Methods in Applied Mechanics and Engineering 272 (2014) 233–250.

[20] M. Tupek, J. Rimoli, R. Radovitzky, An approach for incorporating classical continuum damage models in state-based peridynamics, Computer Methods in Applied Mechanics and Engineering 263 (2013) 20–26.

[21] A. Yaghoobi, M. G. Chorzepa, Meshless modeling framework for fiber reinforced concrete structures, Computers & Structures 161 (2015) 43–54.

[22] A. Yaghoobi, M. G. Chorzepa, Fracture analysis of fiber reinforced concrete structures in the micropolar peridynamic analysis framework, Engineering Fracture Mechanics 169 (2017) 238–250.

[23] S. A. Silling, Linearized theory of peridynamic states, Journal of Elasticity 99 (1) (2010) 85–111.

[24] A. Yaghoobi, M. G. Chorzepa, S. S. Kim, et al., Mesoscale fracture analysis of multiphase cementitious composites using peridynamics, Materials 10 (2) (2017) 162.

[25] J. De Vree, W. Brekelmans, M. Van Gils, Comparison of nonlocal approaches in continuum damage mechanics, Computers & Structures 55 (4) (1995) 581–588.

[26] M. Tupek, R. Radovitzky, An extended constitutive correspondence formulation of peridynamics based on nonlinear bond-strain measures, Journal of the Mechanics and Physics of Solids 65 (2014) 82–92.

[27] A. Yaghoobi, M. G. Chorzepa, Higher-order approximation to suppress the zero-energy mode in non-ordinary state-based peridynamics, Computers & Structures 188 (2017) 63–79.

[28] X. Gu, E. Madenci, Q. Zhang, Revisit of non-ordinary state-based peridynamics, Engineering Fracture Mechanics 190 (2018) 31–52.

[29] P. Li, Z. Hao, W. Zhen, A stabilized non-ordinary state-based peridynamic model, Computer Methods in Applied Mechanics and Engineering 339 (2018) 262–280.

[30] C. Wu, B. Ren, A stabilized non-ordinary state-based peridynamics for the nonlocal ductile material failure analysis in metal machining process, Computer Methods in Applied Mechanics and Engineering 291 (2015) 197–215.

[31] F. Radtke, A. Simone, L. Sluys, A computational model for failure analysis of fibre reinforced concrete with discrete treatment of fibres, Engineering Fracture Mechanics 77 (4) (2010) 597–620.